Appl. Math. Mech. -Engl. Ed., **42**(5), 677–688 (2021)

APPLIED MATHEMATICS AND MECHANICS (ENGLISH EDITION)

https://doi.org/10.1007/s10483-021-2723-9

Effects of surface impedance on current density in a piezoelectric resonator for impedance distribution sensing*

Jing LIU[1,2], Jianke DU[1,†], Ji WANG[1], Jiashi YANG[3]

1. Piezoelectric Device Laboratory, School of Mechanical Engineering and Mechanics, Ningbo University, Ningbo 315211, Zhejiang Province, China;
2. School of Digital Technology and Engineering, Ningbo University of Finance and Economics, Ningbo 315175, Zhejiang Province, China;
3. Department of Mechanical and Materials Engineering, University of Nebraska-Lincoln, Lincoln, NE 68588-0526, U. S. A.

(Received Oct. 10, 2020 / Revised Jan. 27, 2021)

Abstract We study the relationship between the surface mechanical load represented by distributed acoustic impedance and the current density distribution in a shear mode piezoelectric plate acoustic wave resonator. A theoretical analysis based on the theory of piezoelectricity and trigonometric series is performed. In the specific and basic case when the surface load is due to a local mass layer, numerical results show that the current density concentrates under the mass layer and is sensitive to the physical as well as geometric parameters of the mass layer such as its location and size. This provides the theoretical foundation for predicting the surface impedance pattern from the current density distribution, which is fundamental to the relevant acoustic wave sensors.

Key words piezoelectric, resonator, sensor, plate

Chinese Library Classification O343
2010 Mathematics Subject Classification 74J10

1 Introduction

Piezoelectric materials have been used to make acoustic wave resonators as components for oscillators for a long time, from the early quartz crystal resonators (QCRs)[1–2] to the relatively recent film bulk acoustic resonators (FBARs)[3] made from ZnO or AlN. They provide frequency standards for many electronic equipments and are also used as filters for signal processing. They may operate with bulk acoustic waves[4] or surface acoustic waves[5–6]. During the last couple of decades, piezoelectric resonators have also been used extensively to make acoustic wave sensors including mass, fluid, and biological and chemical sensors. Both QCRs[7–12] and

* Citation: LIU, J., DU, J. K., WANG, J., and YANG, J. S. Effects of surface impedance on current density in a piezoelectric resonator for impedance distribution sensing. *Applied Mathematics and Mechanics* (*English Edition*), **42**(5), 677–688 (2021) https://doi.org/10.1007/s10483-021-2723-9

† Corresponding author, E-mail: dujianke@nbu.edu.cn

Project supported by the National Natural Science Foundation of China (Nos. 11672141 and 11972199), the Special Research Funding from the Marine Biotechnology and Marine Engineering Discipline Group in Ningbo University, and the K. C. Wong Magana Fund through Ningbo University

FBARs[13–16] have been used for sensing. QCRs used for sensing are the well-known quartz crystal microbalances (QCMs)[17–20]. Most of these sensors are based on the frequency shifts in the resonators caused by a surface mass layer on contact with a fluid. For the modeling of frequency-based acoustic wave sensors, the frequency perturbation integral[21] of resonators provides the theoretical foundation and a convenient tool for calculating device sensitivity.

Some relatively recent acoustic wave resonator based sensors such as fingerprint sensors[22–29] are used to predict the pattern of the distribution of surface mechanical load that cannot be described by a simple frequency shift. In these sensors, the distribution of the current density in the resonators are often used to measure the distribution of the surface load. The modeling of these sensors presents new challenges. In this paper, we establish theoretically the basic relationship between the small surface load and the current density distribution in a shear mode FBAR. Either the shear mode or the thickness-extensional mode can be used for these applications. We study the shear mode because it is simpler mathematically and is sufficient to show the effect of interest. The equations of piezoelectricity[4] are used. When the surface load is a local mass layer, a trigonometric series solution is obtained. The current density distribution caused by the mass layer is calculated and examined. It is shown that the current density distribution depends on and is sensitive to the physical and geometric parameters of the local mass layer. Hence, the current density distribution can be used to predict the location and size of the mass layer, and more generally, the pattern of more complicated surface load distribution by superposition.

2 Mechanics model

Consider a piezoelectric plate of polarized ceramics or crystals of class (6 mm) (see Fig. 1). The x_3-axis is determined from x_1 and x_2 by the right-hand rule. The plate is unbounded in the x_3-direction. Figure 1 shows a cross-section. We consider unit thickness in the x_3-direction. The plate is electroded on the major faces at $x_2 = \pm h$. The bottom electrodes are small and identical pieces so that the currents on them can be measured separately for their distribution. The bottom electrodes are all grounded. The top electrode is under a time-harmonic driving voltage $V(t)$. The plate is driven into the shear motion described by the displacement field $u_3(x_1, x_2, t)$ through the piezoelectric constant e_{15}. The top surface is loaded mechanically. The specific load of a local mass layer is shown in the figure. The effect of the surface load is described by its acoustic impedance $Z_{23}(x_1)$ in general when the motion is time-harmonic. The two minor faces at $x_1 = \pm a$ are traction free and are unelectroded.

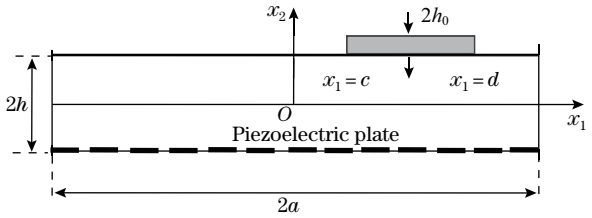

Fig. 1 An electroded piezoelectric plate with surface mechanical load

For crystals of class (6 mm) in motions independent of x_3, the three-dimensional equations of piezoelectricity automatically decouple into two groups for (u_3, φ) and (u_1, u_2), respectively[30–32]. What is relevant to the present paper is the so-called shear-horizontal or anti-plane motions described by $u_3 = u(x_1, x_2, t)$ and $\varphi = \varphi(x_1, x_2, t)$, where φ is the electric potential. A function ψ[30] can be introduced through $\varphi = \psi + eu/\varepsilon$, where $e = e_{15}$ and $\varepsilon = \varepsilon_{11}$ is the relevant dielectric constant. Then, the governing equations for u and ψ are[30–32]

$$\overline{c}\nabla^2 u = \rho u_{,tt}, \quad \nabla^2 \psi = 0, \tag{1}$$

where $\nabla^2 = \partial_1^2 + \partial_2^2$ is the two-dimensional Laplacian, $\overline{c} = c_{44} + e^2/\varepsilon$, and c_{44} is the relevant shear elastic constant. The nonzero stress and electric displacement components are given by

$$\begin{cases} T_{23} = \overline{c}u_{,2} + e\psi_{,2}, \quad T_{31} = \overline{c}u_{,1} + e\psi_{,1}, \\ D_1 = -\varepsilon\psi_{,1}, \quad D_2 = -\varepsilon\psi_{,2}, \end{cases} \tag{2}$$

where an index after a comma denotes the partial differentiation with respect to the coordinate associated with the index. The electrodes are assumed to be very thin. Their mechanical effects are neglected. This is a widely-used approximation for a long time[33–34]. The mechanical effects of the electrodes such as inertia[35–38] and stiffness[39–40] are well-studied and well-understood, and can be included when the electrodes are not thin. For the purpose of this paper, the current density distribution is determined by the mass layer, not the electrodes. Therefore, the consideration of thin electrodes is sufficient. The surface load is described by an impedance distribution $Z_{23}(x_1)$. Then, the boundary conditions can be written as

$$\begin{cases} T_{13} = 0, \quad D_1 = 0, \quad x_1 = \pm a, \\ -T_{23} = Z_{23}u_{,t}, \quad \varphi = V(t), \quad x_2 = h, \\ T_{32} = 0, \quad \varphi = 0, \quad x_2 = -h. \end{cases} \tag{3}$$

When the surface load is simply a mass layer with density ρ', its equation of motion for a differential element of the mass layer is

$$-T_{23} = \rho' 2h' u_{,tt} = \rho' 2h' \mathrm{i}\omega u_{,t}, \tag{4}$$

where h' is the mass layer thickness. From Eqs. (3) and (4), we identify the impedance as

$$Z_{23} = \rho' 2h' \mathrm{i}\omega. \tag{5}$$

The free charge density on the bottom electrode is given by

$$\sigma = D_2. \tag{6}$$

The density of the current flowing out of the bottom electrode is

$$j = -\sigma_{,t}. \tag{7}$$

3 Trigonometric series solution

For time-harmonic motions, we use the following complex notation:

$$(u, \psi, \varphi, V) = \mathrm{Re}((U, \Psi, \Phi, \overline{V}) \exp(\mathrm{i}\omega t)). \tag{8}$$

The real and imaginary parts of the complex amplitude of a field are equivalent to a real amplitude and a phase angle. The real and time-harmonic physical fields are obtained by taking the real parts of the complex fields according to Eq. (8). In terms of U and Ψ, Eqs. (1) and (3) become

$$\overline{c}\nabla^2 U = -\rho\omega^2 U, \quad \nabla^2 \Psi = 0, \tag{9}$$

$$U_{,1} = 0, \quad \Psi_{,1} = 0, \quad x_1 = \pm a, \tag{10}$$

$$\Psi + \frac{e}{\varepsilon} U = \overline{V}, \quad x_2 = h, \tag{11a}$$

$$\overline{c}U_{,2} + e\Psi_{,2} = -Z_{23}\mathrm{i}\omega U, \quad x_2 = h, \tag{11b}$$

$$\Psi + \frac{e}{\varepsilon} U = 0, \quad x_2 = -h, \tag{12a}$$

$$\overline{c} U_{,2} + e\Psi_{,2} = 0, \quad x_2 = -h. \tag{12b}$$

The general solution to Eqs. (9) and (10) can be obtained by separation of variables[31–32],

$$\begin{aligned} U = {} & A_1^{(0)} \cos(\eta_{(0)} x_2) + A_2^{(0)} \sin(\eta_{(0)} x_2) \\ & + \sum_{m=2,4,6,\cdots}^{\infty} (A_1^{(m)} \cos(\eta_{(m)} x_2) + A_2^{(m)} \sin(\eta_{(m)} x_2)) \cos(\xi_{(m)} x_1) \\ & + \sum_{m=1,3,5,\cdots}^{\infty} (A_3^{(m)} \cos(\eta_{(m)} x_2) + A_4^{(m)} \sin(\eta_{(m)} x_2)) \sin(\xi_{(m)} x_1), \end{aligned} \tag{13}$$

$$\begin{aligned} \Psi = {} & B_1^{(0)} + B_2^{(0)} x_2 \\ & + \sum_{m=2,4,6,\cdots}^{\infty} (B_1^{(m)} \cosh(\xi_{(m)} x_2) + B_2^{(m)} \sinh(\xi_{(m)} x_2)) \cos(\xi_{(m)} x_1) \\ & + \sum_{m=1,3,5,\cdots}^{\infty} (B_3^{(m)} \cosh(\xi_{(m)} x_2) + B_4^{(m)} \sinh(\xi_{(m)} x_2)) \sin(\xi_{(m)} x_1), \end{aligned} \tag{14}$$

where

$$\begin{cases} \eta_{(0)}^2 = \dfrac{\rho \omega^2}{\overline{c}}, \\ \xi_{(m)} = \dfrac{m}{2a}\pi, \quad \eta_{(m)}^2 = \dfrac{\rho \omega^2}{\overline{c}} - \left(\dfrac{m}{2a}\pi\right)^2, \quad m = 1, 2, 3, \cdots. \end{cases} \tag{15}$$

$A_1^{(m)}$ through $A_4^{(m)}$ and $B_1^{(m)}$ through $B_4^{(m)}$ are undetermined constants. They need to be determined by the remaining boundary conditions at $x_2 = \pm h$ in Eqs. (11) and (12). This can only be carried out in specific cases. The basic and useful case of a local mass layer will be studied in the next section. Then, more complicated distributions can be predicted by superposition.

4 Case of a local mass layer

The thickness of a local mass layer is given by (see Fig. 1)

$$2h'(x_1) = \begin{cases} 2h_0, & c < x_1 < d, \\ 0, & \text{else}. \end{cases} \tag{16}$$

The substitution of Eqs. (13) and (14) into Eqs. (11a) and (12a) yields the following linear algebraic equations for the undetermined coefficients:

$$\begin{cases} B_1^{(0)} + \dfrac{e}{\varepsilon} A_1^{(0)} \cos(\eta_{(0)} h) = \dfrac{\overline{V}}{2}, \\ B_2^{(0)} h + \dfrac{e}{\varepsilon} A_2^{(0)} \sin(\eta_{(0)} h) = \dfrac{\overline{V}}{2}, \end{cases} \tag{17}$$

$$\begin{cases} B_3^{(m)} \cosh(\xi_{(m)} h) + \dfrac{e}{\varepsilon} A_3^{(m)} \cos(\eta_{(m)} h) = 0, \quad m = 1, 3, 5, \cdots, \\ B_4^{(m)} \sinh(\xi_{(m)} h) + \dfrac{e}{\varepsilon} A_4^{(m)} \sin(\eta_{(m)} h) = 0, \quad m = 1, 3, 5, \cdots, \end{cases} \tag{18}$$

$$\begin{cases} B_1^{(m)} \cosh(\xi_{(m)} h) + \dfrac{e}{\varepsilon} A_1^{(m)} \cos(\eta_{(m)} h) = 0, \quad m = 2, 4, 6, \cdots, \\ B_2^{(m)} \sinh(\xi_{(m)} h) + \dfrac{e}{\varepsilon} A_2^{(m)} \sin(\eta_{(m)} h) = 0, \quad m = 2, 4, 6, \cdots. \end{cases} \tag{19}$$

At the same time, the substitution of Eqs. (13) and (14) into Eqs. (11b) and (12b) yields

$$
\begin{aligned}
&-\overline{c}A_1^{(0)}\eta_{(0)}\sin(\eta_{(0)}h)+\overline{c}A_2^{(0)}\eta_{(0)}\cos(\eta_{(0)}h)+eB_2^{(0)}\\
&+\sum_{m=1,3,5,\cdots}^{\infty}(-\overline{c}A_3^{(m)}\eta_{(m)}\sin(\eta_{(m)}h)+\overline{c}A_4^{(m)}\eta_{(m)}\cos(\eta_{(m)}h)\\
&+eB_3^{(m)}\xi_{(m)}\sinh(\xi_{(m)}h)+eB_4^{(m)}\xi_{(m)}\cosh(\xi_{(m)}h))\sin(\xi_{(m)}x_1)\\
&+\sum_{m=2,4,6,\cdots}^{\infty}(-\overline{c}A_1^{(m)}\eta_{(m)}\sin(\eta_{(m)}h)+\overline{c}A_2^{(m)}\eta_{(m)}\cos(\eta_{(m)}h)\\
&+eB_1^{(m)}\xi_{(m)}\sinh(\xi_{(m)}h)+eB_2^{(m)}\xi_{(m)}\cosh(\xi_{(m)}h))\cos(\xi_{(m)}x_1)\\
=&\,\omega^2\rho' 2h'(A_1^{(0)}\cos(\eta_{(0)}h)+A_2^{(0)}\sin(\eta_{(0)}h)\\
&+\sum_{m=1,3,5,\cdots}^{\infty}(A_3^{(m)}\cos(\eta_{(m)}h)+A_4^{(m)}\sin(\eta_{(m)}h))\sin(\xi_{(m)}x_1)\\
&+\sum_{m=2,4,6,\cdots}^{\infty}(A_1^{(m)}\cos(\eta_{(m)}h)+A_2^{(m)}\sin(\eta_{(m)}h))\cos(\xi_{(m)}x_1)),
\end{aligned}
\tag{20}
$$

$$
\begin{aligned}
&\overline{c}A_1^{(0)}\eta_{(0)}\sin(\eta_{(0)}h)+\overline{c}A_2^{(0)}\eta_{(0)}\cos(\eta_{(0)}h)+eB_2^{(0)}\\
&+\sum_{m=1,3,5,\cdots}^{\infty}(\overline{c}A_3^{(m)}\eta_{(m)}\sin(\eta_{(m)}h)+\overline{c}A_4^{(m)}\eta_{(m)}\cos(\eta_{(m)}h)\\
&-eB_3^{(m)}\xi_{(m)}\sinh(\xi_{(m)}h)+eB_4^{(m)}\xi_{(m)}\cosh(\xi_{(m)}h))\sin(\xi_{(m)}x_1)\\
&+\sum_{m=2,4,6,\cdots}^{\infty}(\overline{c}A_1^{(m)}\eta_{(m)}\sin(\eta_{(m)}h)+\overline{c}A_2^{(m)}\eta_{(m)}\cos(\eta_{(m)}h)\\
&-eB_1^{(m)}\xi_{(m)}\sinh(\xi_{(m)}h)+eB_2^{(m)}\xi_{(m)}\cosh(\xi_{(m)}h))\cos(\xi_{(m)}x_1)\\
=&\,0.
\end{aligned}
\tag{21}
$$

Equations (20) and (21) depend on x_1. To obtain the algebraic equations for the undetermined coefficients, we multiply Eqs. (20) and (21) by $\cos(\xi_{(n)}x_1)$ with $n = 0$, 2, 4 and so on, and integrate them over $[-a, a]$. We also do the same with $\sin(\xi_{(n)}x_1)$ where $n = 1$, 3, 5 and so on. This results in the following linear algebraic equations for the undetermined coefficients:

$$
\begin{aligned}
&(\overline{c}(-A_1^{(0)}\eta_{(0)}\sin(\eta_{(0)}h)+A_2^{(0)}\eta_{(0)}\cos(\eta_{(0)}h))+eB_2^{(0)})2a\\
=&\,\omega^2\rho' 2h_0\Big((A_1^{(0)}\cos(\eta_{(0)}h)+A_2^{(0)}\sin(\eta_{(0)}h))(d-c)\\
&+\sum_{m=1,3,5,\cdots}^{\infty}(A_3^{(m)}\cos(\eta_{(m)}h)+A_4^{(m)}\sin(\eta_{(m)}h))\frac{2a}{m\pi}\left(\cos\left(\frac{m\pi}{2}c\right)-\cos\left(\frac{m\pi}{2}d\right)\right)\\
&+\sum_{m=2,4,6,\cdots}^{\infty}(A_1^{(m)}\cos(\eta_{(m)}h)+A_2^{(m)}\sin(\eta_{(m)}h))\frac{2a}{m\pi}\left(\sin\left(\frac{m\pi}{2}d\right)-\sin\left(\frac{m\pi}{2}c\right)\right)\Big),
\end{aligned}
\tag{22}
$$

$$
\begin{aligned}
&(\overline{c}(-A_3^{(n)}\eta_{(n)}\sin(\eta_{(n)}h)+A_4^{(n)}\eta_{(n)}\cos(\eta_{(n)}h))\\
&+e(B_3^{(n)}\xi_{(n)}\sinh(\xi_{(n)}h)+B_4^{(n)}\xi_{(n)}\cosh(\xi_{(n)}h)))a\\
=&\,\omega^2\rho' 2h_0\Big((A_1^{(0)}\cos(\eta_{(0)}h)+A_2^{(0)}\sin(\eta_{(0)}h))\frac{2a}{n\pi}\Big(\cos\Big(\frac{n\pi}{2a}c\Big)-\cos\Big(\frac{n\pi}{2a}d\Big)\Big)\\
&+\sum_{m=1,3,5,\cdots}^{\infty}(A_3^{(m)}\cos(\eta_{(m)}h)+A_4^{(m)}\sin(\eta_{(m)}h))\frac{a}{(m+n)\pi}\Big(\sin\Big(\frac{(m+n)\pi}{2a}c\Big)\\
&-\sin\Big(\frac{(m+n)\pi}{2a}d\Big)\Big)+\sum_{\substack{m=1,3,5,\cdots\\ m=n}}^{\infty}(A_3^{(m)}\cos(\eta_{(m)}h)+A_4^{(m)}\sin(\eta_{(m)}h))\frac{1}{2}(d-c)\\
&+\sum_{\substack{m=1,3,5,\cdots\\ m\neq n}}^{\infty}(A_3^{(m)}\cos(\eta_{(m)}h)+A_4^{(m)}\sin(\eta_{(m)}h))\frac{a}{(m-n)\pi}\Big(\sin\Big(\frac{(m-n)\pi}{2a}d\Big)\\
&-\sin\Big(\frac{(m-n)\pi}{2a}c\Big)\Big)+\sum_{m=2,4,6,\cdots}^{\infty}(A_1^{(m)}\cos\eta_{(m)}h+A_2^{(m)}\sin(\eta_{(m)}h))\\
&\cdot\Big(-\frac{a}{(m+n)\pi}\Big(\cos\Big(\frac{(m+n)\pi}{2a}d\Big)-\cos\Big(\frac{(m+n)\pi}{2a}c\Big)\Big)\\
&+\frac{a}{(m-n)\pi}\Big(\cos\Big(\frac{(m-n)\pi}{2a}d\Big)-\cos\Big(\frac{(m-n)\pi}{2a}c\Big)\Big)\Big)\Big),\quad n=1,3,5,\cdots,
\end{aligned}
\tag{23}
$$

$$
\begin{aligned}
&(\overline{c}(-A_1^{(n)}\eta_{(n)}\sin(\eta_{(n)}h)+A_2^{(n)}\eta_{(n)}\cos(\eta_{(n)}h))\\
&+e(B_1^{(n)}\xi_{(n)}\sinh(\xi_{(n)}h)+B_2^{(n)}\xi_{(n)}\cosh(\xi_{(n)}h)))a\\
=&\,\omega^2\rho' 2h_0\Big((A_1^{(0)}\cos(\eta_{(0)}h)+A_2^{(0)}\sin(\eta_{(0)}h))\frac{2a}{n\pi}\Big(\sin\Big(\frac{n\pi}{2a}d\Big)-\sin\Big(\frac{n\pi}{2a}c\Big)\Big)\\
&+\sum_{m=1,3,5,\cdots}^{\infty}(A_3^{(m)}\cos(\eta_{(m)}h)+A_4^{(m)}\sin(\eta_{(m)}h))\Big(\frac{a}{(m+n)\pi}\Big(\cos\Big(\frac{(m+n)\pi}{2a}c\Big)\\
&-\cos\Big(\frac{(m+n)\pi}{2a}d\Big)\Big)+\frac{a}{(m-n)\pi}\Big(\cos\Big(\frac{(m-n)\pi}{2a}c\Big)-\cos\Big(\frac{(m-n)\pi}{2a}d\Big)\Big)\Big)\\
&+\sum_{m=2,4,6,\cdots}^{\infty}(A_1^{(m)}\cos(\eta_{(m)}h)+A_2^{(m)}\sin(\eta_{(m)}h))\frac{a}{(m+n)\pi}\Big(\sin\Big(\frac{(m+n)\pi}{2a}d\Big)\\
&-\sin\Big(\frac{(m+n)\pi}{2a}c\Big)\Big)+\sum_{\substack{m=2,4,6,\cdots\\ m=n}}^{\infty}\Big(A_1^{(m)}\cos(\eta_{(m)}h)+A_2^{(m)}\sin(\eta_{(m)}h)\Big)\frac{1}{2}(d-c)\\
&+\sum_{\substack{m=2,4,6,\cdots\\ m\neq n}}^{\infty}(A_1^{(m)}\cos(\eta_{(m)}h)+A_2^{(m)}\sin(\eta_{(m)}h))\frac{a}{(m-n)\pi}\Big(\sin\Big(\frac{(m-n)\pi}{2a}d\Big)\\
&-\sin\Big(\frac{(m-n)\pi}{2a}c\Big)\Big)\Big),\quad n=2,4,6,\cdots,
\end{aligned}
\tag{24}
$$

$$
\overline{c}(A_1^{(0)}\eta_{(0)}\sin(\eta_{(0)}h)+A_2^{(0)}\eta_{(0)}\cos(\eta_{(0)}h))+eB_2^{(0)}=0,
\tag{25}
$$

$$\overline{c}(A_3^{(n)}\eta_{(n)}\sin(\eta_{(n)}h) + A_4^{(n)}\eta_{(n)}\cos(\eta_{(n)}h)) + e(-B_3^{(n)}\xi_{(n)}\sinh(\xi_{(n)}h) + B_4^{(n)}\xi_{(n)}\cosh(\xi_{(n)}h)) = 0, \quad n = 1, 3, 5, \cdots, \tag{26}$$

$$\overline{c}(A_1^{(n)}\eta_{(n)}\sin(\eta_{(n)}h) + A_2^{(n)}\eta_{(n)}\cos(\eta_{(n)}h)) + e(-B_1^{(n)}\xi_{(n)}\sinh(\xi_{(n)}h) + B_2^{(n)}\xi_{(n)}\cosh(\xi_{(n)}h)) = 0, \quad n = 2, 4, 6, \cdots. \tag{27}$$

Equations (22)–(27) and (17)–(19) form a complete system of linear algebraic equations for the undetermined coefficients. They are solved on a computer. Then, according to Eq. (7), the current density of interest can be calculated from

$$j = \mathrm{i}\omega\varepsilon\Big(B_2^{(0)} + \sum_{m=2,4,6,\cdots}^{\infty} \xi_{(m)}(B_1^{(m)}\sinh(\xi_{(m)}x_2) + B_2^{(m)}\cosh(\xi_{(m)}x_2))\cos(\xi_{(m)}x_1) + \sum_{m=1,3,5,\cdots}^{\infty} \xi_{(m)}(B_3^{(m)}\sinh(\xi_{(m)}x_2) + B_4^{(m)}\cosh(\xi_{(m)}x_2))\sin(\xi_{(m)}x_1)\Big). \tag{28}$$

5 Numerical results for a local mass layer

For numerical results, consider an AlN[41] resonator with $\rho = 3.26 \times 10^3\,\mathrm{kg/m^3}$ and $c_{44} = 118 \times 10^9\ (1 + \mathrm{i}/Q)\,\mathrm{N/m^2}$, where i is the imaginary unit, and Q is the material quality factor. A complex elastic constant is used to include material damping. For AlN, the value of Q ranges from 100 to 700[42–44]. It describes the material damping only. Real devices have other origins of damping such as air resistance and energy leaking at mounting points. Therefore, a larger value of $Q = 50$ is used in the calculations below as a representation of the total damping. The piezoelectric constants $e = e_{15} = -0.48\,\mathrm{C/m^2}$. The dielectric constant $\varepsilon = \varepsilon_{11} = 8.0 \times 10^{-11}\,\mathrm{F/m}$. The resonator length $2a = 200\,\mu\mathrm{m}$, and the thickness $2h = 1\,\mu\mathrm{m}$[45–47]. The local mass layer is within (c, d). The mass ratio between the mass layer and the crystal plate is described by

$$R' = \rho' 2h_0/(\rho 2h).$$

Some of the above parameters will be varied and specified later in individual figures. We use the following fundamental shear resonance frequency of an unbounded AlN plate as a frequency unit:

$$\omega_0 = \frac{\pi}{2h}\sqrt{\frac{\overline{c}}{\rho}}\,. \tag{29}$$

The actual resonance frequency of the resonator in our numerical example is slightly below Eq. (29) because of the inertia of the surface mass layer.

Numerical tests show that the trigonometric series converges rapidly. With 58 or 60 terms, the absolute values of the displacement distributions at the plate bottom shown in Fig. 2 are indistinguishable. Therefore, 60 terms are used for the rest of the calculations. The displacement is large under the mass layer and decays quickly outside the mass layer edges. This is the so-called energy trapping effect of mass layers in resonators. It can be seen that there are some small oscillations near the edges of the local mass layer. This is because a local mass layer is described by a piecewise constant function (see Eq. (16)) with finite discontinuities at the mass layer edges where a trigonometric series converges with oscillations (Gibbs phenomenon).

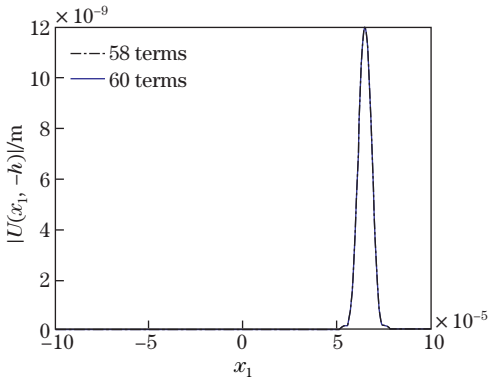

Fig. 2 Displacement distribution showing convergence when $c = 60\,\mu\text{m}$, $d = 70\,\mu\text{m}$, $R' = 0.02$, $\overline{V} = 2\,\text{V}$, and $Q = 50$ (color online)

Figure 3 shows the effects of the mass layer location on the displacement distribution at the bottom of the resonator. The real and imaginary parts as well as the absolute value of the complex displacement are all presented for complete understanding. This figure suggests the possibility of measuring the location of the mass layer through vibration distribution, which can be realized electrically using the related current density distribution as to be seen in the following content.

Figure 4 shows the effects of the mass layer location on the current density distribution at

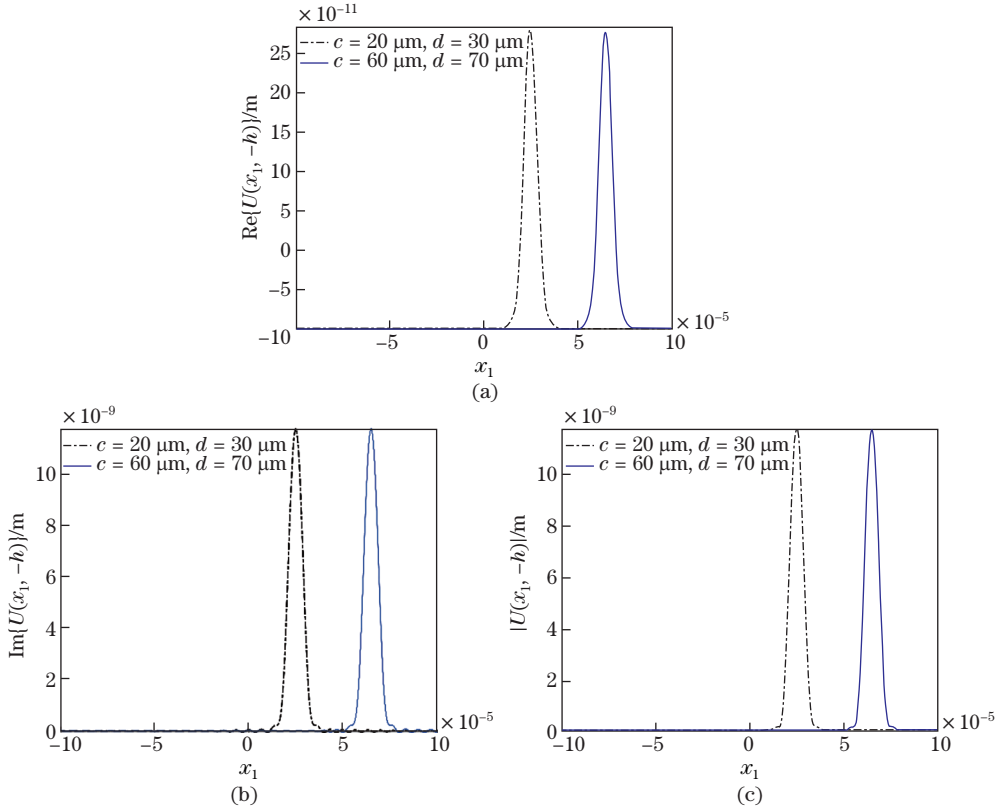

Fig. 3 Effects of mass layer location (c, d) on displacement distribution: (a) real part, (b) imaginary part, and (c) absolute value, when $R' = 0.02$, $\overline{V} = 2\,\text{V}$, and $Q = 50$ (color online)

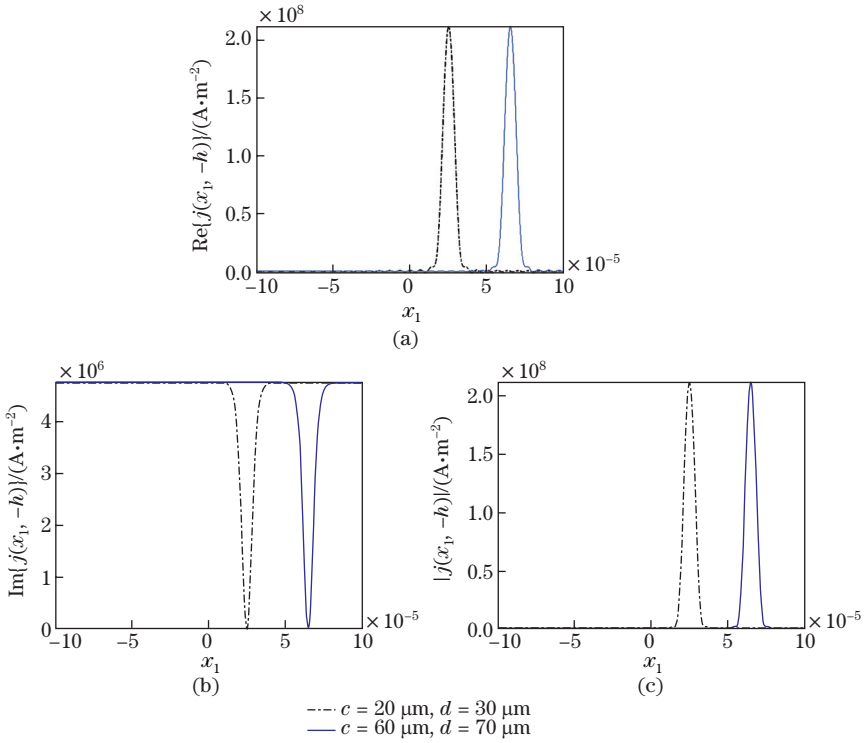

Fig. 4 Effects of mass layer location (c, d) on current density distribution: (a) real part, (b) imaginary part, and (c) absolute value, when $R' = 0.02$, $\overline{V} = 2\,\mathrm{V}$, and $Q = 50$ (color online)

the bottom of the resonator, which is the main result of the present paper. It can be seen that the current density is the maximal under the mass layer. More generally, if there are several local mass layers at different locations, it is reasonable to expect several corresponding peaks of the current density distribution. Hence, there is correspondence between the surface impedance distribution and the current density distribution. This provides the theoretical foundation for measuring the surface mechanical load distribution pattern through the current density distribution.

Figure 5 shows the effects of various physical and geometric parameters on the current density distribution. In Fig. 5(a), the current density increases as the driving voltage increases, which is as expected from the linear theory used. Figure 5(b) shows that for a larger Q or less damping, the current density is larger because of stronger vibration. When the mass layer is wider, so is the current density, as shown in Fig. 5(c). When the mass layer is heavier, the current density becomes smaller, as shown in Fig. 5(d).

6 Conclusions

The relationship between a surface local mass layer and the current density distribution at the bottom electrodes is established. The current density is large under the mass layer and is sensitive to its geometric and physical parameters. Thus, the current density distribution is closely related to the pattern of the surface mass layer or acoustic impedance distribution in general, and can be used to measure the surface impedance pattern. This provides the basic understanding of the mechanism of a class of acoustic wave sensors.

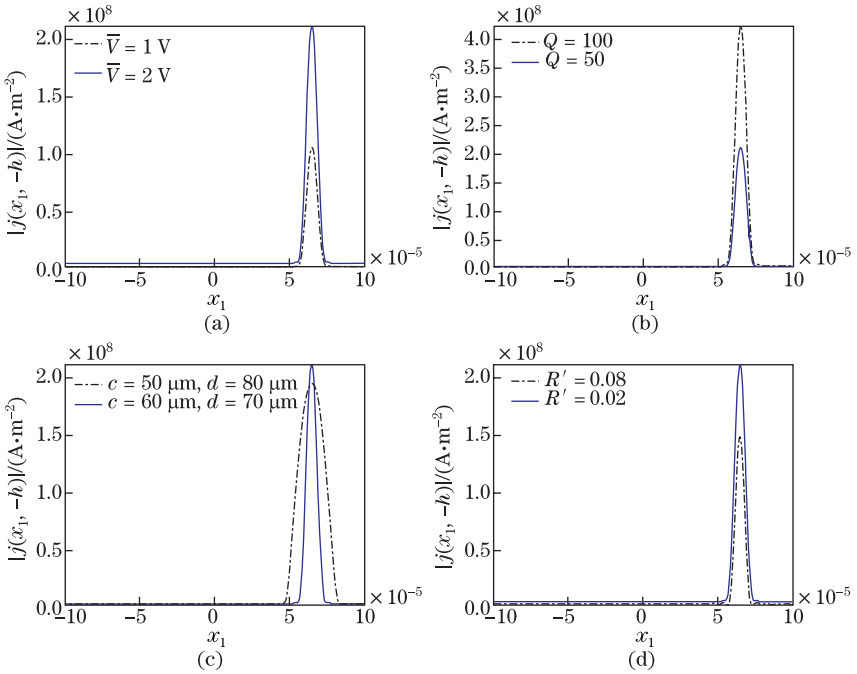

Fig. 5 Effects of (a) $\overline{V}$, (b) Q, (c) mass layer size, and (d) mass layer inertia on current density distribution, when $c = 60\,\mu\text{m}$, $d = 70\,\mu\text{m}$, $R' = 0.02$, $\overline{V} = 2\,\text{V}$, and $Q = 50$ unless varied (color online)

References

[1] BOTTOM, V. E. *Introduction to Quartz Crystal Unit Design*, Van Nostrand Reinhold, New York (1982)

[2] SALT, D. *Hy-Q Handbook of Quartz Crystal Devices*, Van Nostrand Reinhold, Berkshire (1987)

[3] LAKIN, K. M. A review of thin-film resonator technology. *IEEE Microwave Magazine*, **4**(2), 61–67 (2003)

[4] TIERSTEN, H. F. *Linear Piezoelectric Plate Vibrations*, Plenum, New York (1969)

[5] CAMPBELL, C. K. *Surface Acoustic Wave Devices for Mobile and Wireless Communications*, Academic Press, Orlando (1998)

[6] HASHIMOTO, K. Y. *Surface Acoustic Wave Devices in Telecommunications*, Springer, Berlin (2000)

[7] SAUERBREY, G. Verwendung von schwingquarzen zur wägung dünner schichten und zur mikrowägung. *Ztschrift Für Physik*, **155**(2), 206–222 (1959)

[8] KANAZAWA, K. K. and GORDON II, J. G. The oscillation frequency of a quartz resonator in contact with a fluid. *Analytica Chimica Acta*, **175**, 99–105 (1985)

[9] REED, C. E., KANAZAWA, K. K., and KAUFMAN, J. H. Physical description of a viscoelastically loaded AT-cut quartz resonator. *Journal of Applied Physics*, **68**(5), 1993–2001 (1990)

[10] MARTIN, S. J., GRANSTAFF, V. E., and FRYE, G. C. Characterization of a quartz crystal microbalance with simultaneous mass and liquid loading. *Analytical Chemistry*, **63**(20), 2272–2281 (1991)

[11] DUNCAN-HEWITT, W. C. and THOMPSON, M. Four-layer theory for the acoustic shear wave sensor in liquids incorporating interface slip and liquid structure. *Analytical Chemistry*, **64**(1), 94–105 (1992)

[12] JING, Y., CHEN, J., CHEN, X., and GONG, X. Frequency shift of thickness-shear vibrations of AT-cut quartz resonators due to a liquid layer with the electrode stiffness considered. *IEEE Transactions on Ultrasonics*, *Ferroelectrics*, *and Frequency Control*, **54**(7), 1290–1292 (2007)

[13] LINK, M., SCHREITER, M., WEBER, J., PRIMIG, R., PITZER, D., and GABL, R. Solidly mounted ZnO shear mode film bulk acoustic wave resonators for sensing applications in liquids. *IEEE Transactions on Ultrasonics*, *Ferroelectrics*, *and Frequency Control*, **53**(2), 492–496 (2006)

[14] FU, Y. Q., LUO, J. K., DU, X. Y., FLEWITT, A. J., LI, Y., MARKX, G. H., WALTON, A. J., and MILNE, W. I. Recent developments on ZnO films for acoustic wave based bio-sensing and microfluidic applications: a review. *Sensors & Actuators B*: *Chemical*, **143**(2), 606–619 (2010)

[15] ZHANG, Y. and BAO, Y. Sensitivity analysis of multi-layered C-axis inclined zigzag zinc oxide thin-film resonators as viscosity sensors. *IEEE Transactions on Ultrasonics*, *Ferroelectrics*, *and Frequency Control*, **61**(3), 525–534 (2014)

[16] LIU, J., DU, J. K., WANG, J., and YANG, J. S. Thin film bulk acoustic wave piezoelectric resonators with circular ring driving electrodes for mass sensing. *Integrated Ferroelectrics*, **192**(1), 57–66 (2018)

[17] CUMPSON, P. J. and SEAH, M. P. The quartz crystal microbalances; radial/polar dependence of mass sensitivity both on and off the electrodes. *Measurement Science & Technology*, **1**(7), 544–555 (1990)

[18] TATSUMA, T., WATANABE, Y., and OYAMA, N. Multichannel quartz crystal microbalances. *Analytical Chemistry*, **71**(17), 3632–3636 (1999)

[19] SHEN, F. and LU, P. Influence of interchannel spacing on the dynamical properties of multichannel quartz crystal microbalance. *IEEE Transactions on Ultrasonics*, *Ferroelectrics*, *and Frequency Control*, **50**(6), 668–675 (2003)

[20] LIU, N., YANG, J. S., WANG, J., and KOSINSKI, J. A. Analysis of a monolithic, nonperiodic array of quartz crystal microbalances. *Japanese Journal of Applied Physics*, **52**(7), 77301 (2013)

[21] TIERSTEN, H. F. Perturbation theory for linear electroelastic equations for small fields superposed on a bias. *The Journal of the Acoustical Society of America*, **64**(3), 832–837 (1978)

[22] LU, Y. P., TANG, H. Y., FANG, S., and WANG, Q. Ultrasonic fingerprint sensor using a piezoelectric micromachined ultrasonic transducer array integrated with complementary metal oxide semiconductor electronics. *Applied Physics Letters*, **106**, 263503 (2015)

[23] PARK, H. and ROH, Y. Design of ultrasonic fingerprint sensor made of 1–3 piezocomposites by finite element method. *Japanese Journal of Applied Physics*, **56**(1), 07JD06 (2017)

[24] BICZ, W., GUMIENNY, Z., and PLUTA, M. Ultrasonic sensor for fingerprints recognition. *Proceedings of SPIE — The International Society for Optics and Photonics*, **2634**, 104–111 (1995)

[25] CHOI, W. Y., KANG, K. C., and PARK, K. K. Ultrasonic fingerprint sensor in underglass prototype using impedance mismatching. *Journal of Mechanical Science and Technology*, **34**(2), 1–9 (2020)

[26] FUNG, S., LU, Y., TANG, H. Y., TSAI, J. M., DANEMAN, M., BOSER, B. E., and HORSLEY, D. A. Theory and experimental analysis of scratch resistant coating for ultrasonic fingerprint sensors. 2015 *IEEE International Ultrasonics Symposium*, IEEE, Taipei (2015)

[27] JIANG, X. Y., TANG, H. Y., LU, Y., NG, E. J., TSAI, J. M., BOSER, B. E., and HORSLEY, D. A. Ultrasonic fingerprint sensor with transmit beam forming based on a PMUT array bonded to CMOS circuitry. *IEEE Transactions on Ultrasonics*, *Ferroelectrics*, *and Frequency Control*, **64**(9), 1401–1408 (2017)

[28] SCHMITT, R. M., ZEICHMAN, J., CASANOVA, A. C., and DELONG, D. Model based development of a commercial, acoustic fingerprint sensor. 2012 *IEEE International Ultrasonics Symposium*, IEEE, Dresden (2012)

[29] TANG, H. Y., LU, Y., JIANG, X., NG, E. J., TSAI, J. M., HORSLEY, D. A., and BOSER, B. E. 3-D ultrasonic fingerprint sensor-on-a-chip. *IEEE Journal of Solid-State Circuits*, **51**(11), 2522–2533 (2016)

[30] BLEUSTEIN, J. L. A new surface wave in piezoelectric materials. *Applied Physics Letters*, **13**(12), 412–413 (1968)

[31] YANG, J. S., CHEN, Z. G., and HU, Y. T. Vibration of a thickness-twist mode piezoelectric resonator with asymmetric, non-uniform electrodes. *IEEE Transactions on Ultrasonics, Ferroelectrics, and Frequency Control*, **55**(4), 841–848 (2008)

[32] YANG, J. S. *Antiplane Motions of Piezoceramics and Acoustic Wave Devices*, World Scientific, Singapore (2010)

[33] TIERSTEN, H. F. Wave propagation in an infinite piezoelectric plate. *Journal of the Acoustical Society of America*, **35**, 234–239 (1963)

[34] YANG, J. S. *Vibration of Piezoelectric Crystal Plates*, World Scientific, Singapore (2013)

[35] TIERSTEN, H. F. and STEVENS, D. S. An analysis of thickness-extensional trapped energy resonant device structures with rectangular electrodes in the piezoelectric thin film on silicon configuration. *Journal of Applied Physics*, **54**(10), 5893–5910 (1983)

[36] ZHAO, Z. N., QIAN, Z. H., WANG, B., and YANG, J. S. Energy trapping of thickness-extensional modes in thin film bulk acoustic wave resonators. *Journal of Mechanical Science and Technology*, **29**(7), 2767–2673 (2015)

[37] ZHAO, Z. N., QIAN, Z. H., and WANG, B. Energy trapping of thickness-extensional modes in thin film bulk acoustic wave filters. *AIP Advances*, **6**(1), 993–995 (2016)

[38] ZHAO, Z. N., QIAN, Z. H., and WANG, B. Vibration optimization of ZnO thin film bulk acoustic resonator with ring electrodes. *AIP Advances*, **6**(4), 1735–1739 (2016)

[39] YANG, J. S., ZHOU, H. G., and ZHANG, W. P. Thickness-shear vibration of rotated Y-cut quartz plates with relatively thick electrodes of unequal thickness. *IEEE Transactions on Ultrasonics, Ferroelectrics, and Frequency Control*, **52**(5), 918–922 (2005)

[40] DU, J. K., XIAN, K., WANG, J., and YANG, J. S. Thickness vibration of piezoelectric plates of 6 mm crystals with tilted six-fold axis and two-layered thick electrodes. *Ultrasonics*, **49**(2), 149–152 (2009)

[41] AULD, B. A. *Acoustic Fields and Waves in Solids*, John Wiley and Sons, New York (1973)

[42] KUMAR, Y., RANGRA, K., and AGARWAL, R. Design and simulation of FBAR for quality factor enhancement. *MAPAN-Journal of Metrology Society of India*, **32**, 113–119 (2017)

[43] KHINE, L., WONG, L. Y. L., SOON, J. B. W., and TSAI, J. M. FBAR resonators with sufficient high Q for RF filter implementation. *Advanced Materials Research*, **254**, 70–73 (2011)

[44] TAY, K. W., HUANG, C. L., and WU, L. Highly c-axis oriented thin AlN films deposited on gold seed layer for FBAR devices. *Journal of Vacuum Science & Technology B*, **23**(4), 1474–1479 (2005)

[45] YANG, C. M., UEHARA, K., KIM, S. K., and KAMEDA, S. Highly c-axis-oriented AlN film using MOCVD for 5 GHz-band FBAR filter. 2003 *IEEE Ultrasonics Symposium Proceedings*, IEEE, New York, 171–173 (2003)

[46] WINGQVIST, G., YANTCHEV, V., and KATARDJIEV, I. Mass sensitivity of multilayer thin film resonant BAW sensors. *Sensors & Actuators A: Physical*, **148**(1), 88–95 (2008)

[47] ZHOU, C. J., YANG, Y., SHY, Y., CAI, H. L., REN, T. L., CHAN, M., ZHOU, J., JIN, H., DONG, S. R., and YANG, C. Y. Visible-light photoresponse of AlN-based film bulk acoustic wave resonator. *Applied Physics Letters*, **102**(19), 1–3 (2013)